Fusion Engineering and Design 85 (2010) 752–760

Contents lists available at ScienceDirect

Fusion Engineering and Design

journal homepage: www.elsevier.com/locate/fusengdes

Quench analysis of an ITER TF coil

R. Zanino[a,*], D. Bessette[b], L. Savoldi Richard[a]

[a] Dipartimento di Energetica, Politecnico de Torino, I-10129 Torino, Italy
[b] ITER Organization, Cadarache, France

ARTICLE INFO

Article history:
Received 1 April 2010
Received in revised form 20 April 2010
Accepted 21 April 2010
Available online 15 May 2010

Keywords:
Nuclear fusion
ITER
Superconducting coils
Quench
Computational codes

ABSTRACT

The first realistic application of the recently developed 4C code is presented, aimed at showing its capability to simulate in an integrated fashion relevant transients for the superconducting coil operation in the International Thermonuclear Experimental Reactor (ITER), both at the system and at the conductor levels. The quench initiation and propagation in an ITER TF coil is considered, including the coil fast discharge phase until the opening of the relief valves. The 14 coil pancakes cooled by alternating clockwise/counter-clockwise SHe flow, the radial plates and the case, the 96 case cooling channels, and the external cryogenic circuit up to the LHe bath are included in the model. The results of the analysis are discussed with particular reference to quench propagation in the winding, hot spot temperature and peak pressurization, mass flow rate evolution in the different system components. The accuracy of the analysis is guaranteed by suitable convergence studies.

© 2010 Elsevier B.V. All rights reserved.

1. Introduction

Within the framework of the International Thermonuclear Experimental Reactor (ITER) activities, most of the "macro"-scale analysis of the superconducting coil operation, see e.g. [1], was performed so far with the Vincenta code, developed in the past for the analysis of the thermal–hydraulic behaviour of superconducting magnet systems used for various applications; other tools, e.g., the Mithrandir code [2], were developed and applied for the "micro"-scale analysis at the conductor level. "Meso"-scale tools were also developed, e.g. the M&M code [3], and applied to the thermal–hydraulic analysis of the whole winding, whenever either the structures themselves [4] or their role in the considered transients [5] were negligible.

Very recently, a novel tool, the 4C code, has been developed for the thermal–hydraulic analysis of the ITER coil system from the conductor level up to the LHe bath [6,7].

Here we present the first realistic application of the 4C code aimed at showing its capability to simulate transients in an integrated fashion at both the system and the conductor levels. This implies that very different (separate) space and time scales have to be simultaneously modeled in an accurate way. The most critical and arguably most relevant such transient is considered, namely the quench initiation and propagation in an ITER TF coil, including the coil fast discharge; this requires, for instance, the use of an adaptive grid following the quench front propagation *in each conductor*. The results of the analysis will be presented with particular reference to quench propagation in the winding, hot spot temperature and pressurization, maximum temperature in the radial plate/case, mass flow rate evolution in the different system components.

2. Overview of ITER TF coils and 4C code

The ITER TF coil and the respective cooling circuit are shown schematically in Fig. 1. The coil is pancake wound using dual channel cable-in-conduit conductors typical of ITER [8]. In both the winding pack cooling loop and the case cooling loop the relief valves are located at inlet and outlet of each of the coils.

The 4C code structure and the corresponding model of an ITER TF coil and cooling circuit have been already presented in [6,7], so that we do not repeat all of those details here. However, for the sake of clarity, we report in Fig. 2 a schematic of the winding and case cooling circuit models used for the present analysis (notice that no manifolds at the coil inlet/outlet are included in the model at present). The parameters characterizing the main circuit components for the present exercise are summarized in Table 1. The pumps are assumed to have a linear characteristic (flow rate vs. pressure head).

Several improvements have been implemented with respect to the model presented in [7]:

- the full detail of the He circulation in the winding, including alternating clockwise and counter-clockwise flow directions in neighbouring pancakes;

* Corresponding author. Tel.: +39 0110904490.
E-mail address: roberto.zanino@polito.it (R. Zanino).

0920-3796/$ – see front matter © 2010 Elsevier B.V. All rights reserved.
doi:10.1016/j.fusengdes.2010.04.056

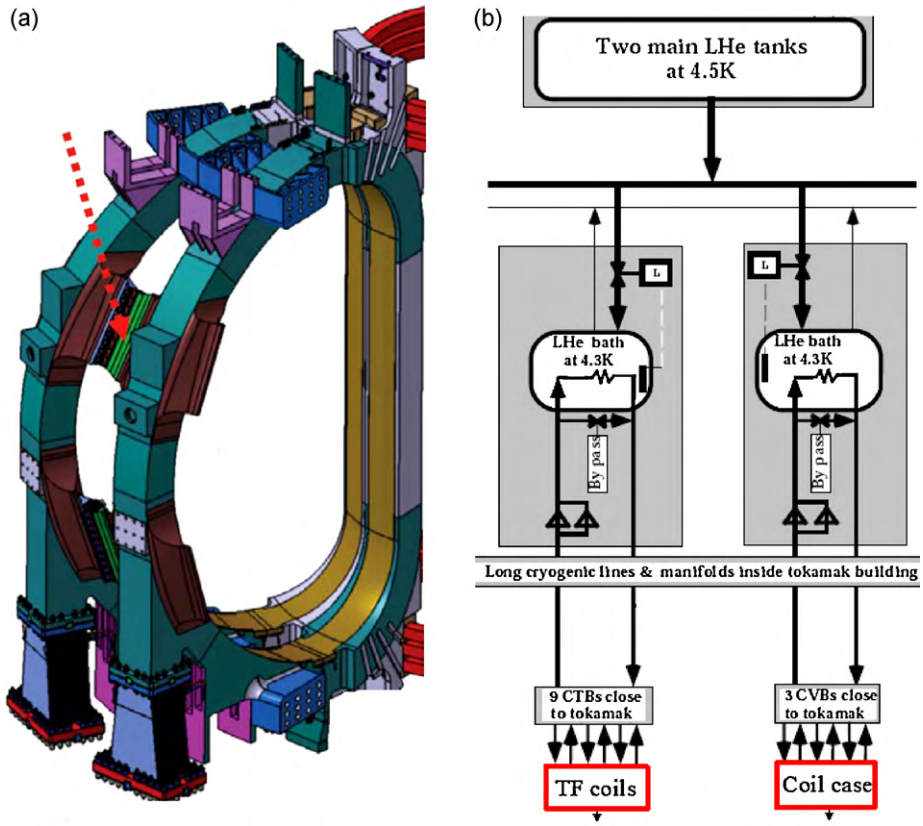

Fig. 1. (a) ITER TF coils (reproduced from [8]) and (b) respective part of the cooling circuit (reproduced from [9]).

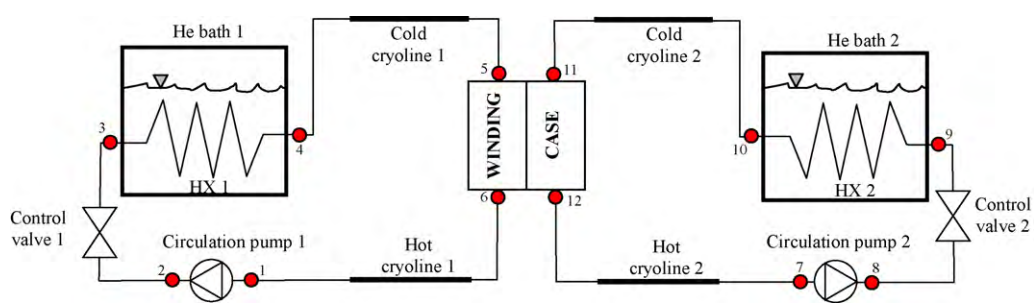

Fig. 2. Schematic of winding and case cooling circuit models. Two control valves are present but not operated during the transient. Different nodes/locations are indicated to be used in Table 4.

Table 1
Parameters characterizing the main circuit components.

Circuit	Component	Parameter	Value
Winding	Pump 1	Flow rate @ zero pressure increase (kg/s)	0.20
		Pressure increase @ zero flow (MPa)	0.50
Winding/case	HX	Length (m)	31.00
		Diameter (m)	0.040
		Heat transfer coefficient (W/m^2K)	1000.00
	He bath	Temperature (K)	4.20
	Cold cryoline	Length (m)	110.00
		Diameter (m)	0.080
	Hot cryoline	Length (m)	110.00
		Diameter (m)	0.080
Case	Pump 2	Flow rate @ zero pressure increase (kg/s)	0.8
		Pressure increase @ zero flow (MPa)	0.7

- all (96) case cooling channels are considered;
- an arbitrary number N_{CUTS} of 2D cuts (up to 16 in the present case, as shown in Fig. 3) for the poloidal discretization of the originally 3D heat conduction problem in the structures.

3. TF quench analysis

3.1. Definition of the problem

To initiate the quench we apply a localized (1 m, 200 ms) square wave heat pulse at the location which is characterized by the minimum $\Delta T \equiv T_{CS} - T_{op}$ margin inside the coil (T_{CS} is the current sharing temperature and T_{op} is the operational temperature). The minimum margin location is identified accounting for both the magnetic field and the strain distributions, see below, computed at the end-of-burn in the reference ITER inductive operation scenario.

The (un-protected) quench propagation is simulated until time $t = t_{0.1} + \tau_{delay}$, where $t_{0.1}$ is the time when the computed voltage across the coil reaches 0.1 V and $\tau_{delay} = 2$ s accounts for the delay in

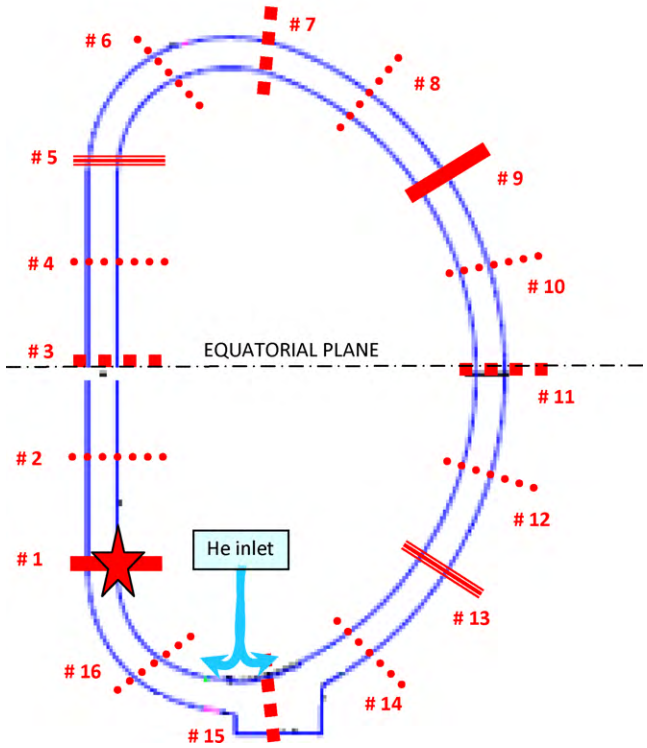

Fig. 3. Sketch of the TF coil with $N_{CUTS} = 16$. In the simulations with $N_{CUTS} = 2$, only the cuts corresponding to the thick solid lines were considered; simulations with $N_{CUTS} = 4$ use additionally the cuts represented with three lines; simulations with $N_{CUTS} = 8$ use additionally the cuts represented with thick dashed lines. The location of the helium inlet is also indicated (flow is counter-clockwise in odd pancakes and clockwise in even pancakes), as well as the location (big star) of the heated region in pancake #7.

the response of the coil protection system; at this time the current is dumped (fast discharge). During the fast discharge the current deviates from the initial exponential decay with time constant equal to 11 s, due to the magnetic coupling to the surrounding structures (vacuum vessel, TF case and radial plates).

The current dump gives rise to a significant heat deposition by dissipation of eddy currents both in the radial plates (q_rp) and in the case (q_case), which in turn pressurizes the circuit. When the pressure at one of the coil/cooling channels end reaches 18 bar, the relief valve opens and the simulation is stopped.

Table 2
TF strand parameters used in the simulations.

Superconducting (SC) material	Nb_3Sn
# of strands (SC, Cu)	900, 522
⌀ strand (SC and Cu)	0.82 mm
Cu: non-Cu (SC strands)	1.0
RRR	100
Cabling pattern	((2 SC + 1 Cu) × 3 × 5 × 5 + core) × 6
$\cos\theta$	0.95
SC properties (Summers scaling)	$T_{c0\,m} = 18$ K, $B_{c20\,m} = 28$ T, $C_{00} = 1.303e10$ A/mm^2

Table 3
TF conductor parameters used in the simulations.

Conductor/pancake lengths (m)	
P3–P12	363
P2, P13	297
P1, P14	99
Void fraction	33.2%
⌀ central channel (ID /OD) (mm)	7/9
Nominal spiral perforation	25%
⌀ jacket (ID /OD) (mm)	40.5/43.7
Jacket material	316LN
Petal wrapping wetted perimeter (mm)	330
Cable n-value	7

3.2. Simulation setup and input

In the reference case $N_{CUTS} = 16$ is used (see Fig. 3) in order to discretize in the poloidal direction the 3D heat conduction problem in the structures. For the sake of simplicity, the coil cross-sections on half of the cuts are assumed to have the same (swaged) profile – so-called inboard section, while the other half are assumed to have the same (rectangular) profile – so-called outboard section (in principle the code could however deal with a different arbitrary cross-section for each of the cuts). The sensitivity of the simulation results to the value chosen for N_{CUTS} has been separately checked as discussed in Appendix.

The input needed for the simulation includes:

- The strand and conductor data, collected below in Tables 2 and 3, respectively.
- The map of the average (on the cross-section) magnetic field distribution $B(x)$ along the odd pancakes, shown in Fig. 4, was provided by a separate computation [1], while the map for the even pancakes (Fig. 4) has been deduced here by symmetry considerations (here x is the coordinate measured from the helium inlet); the field distribution on all odd (even) pancakes is assumed to be the same for the sake of simplicity. The resulting strain maps $\varepsilon(x)$

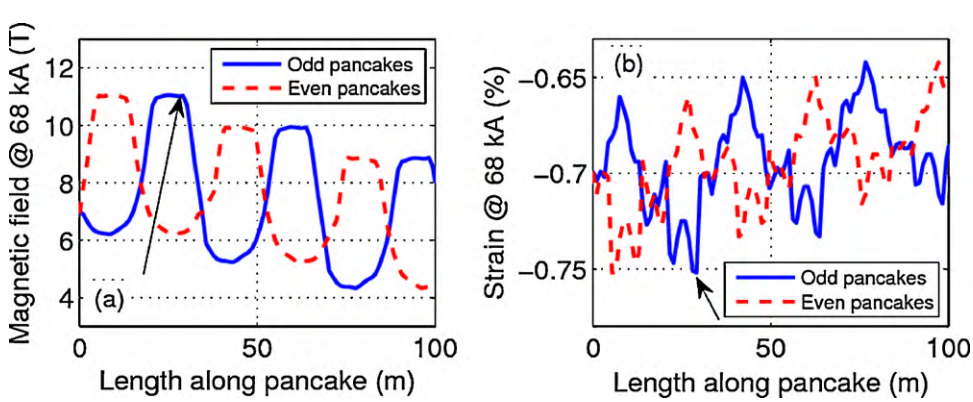

Fig. 4. (a) Average magnetic field and (b) strain distribution along the first turns of odd (solid) and even (dashed) pancakes, respectively. The arrows indicate the location where the disturbance inducing the quench is applied in the simulation, corresponding to the hydraulic end of the TF straight leg (see also Fig. 3).

have been computed assuming that $\varepsilon = \varepsilon_{th} + \varepsilon_{op} + \varepsilon_{extra}$ [10] and the corresponding distribution is also shown in Fig. 4. The most critical location, where the disturbance initiating the quench shall be applied is at $x \sim 30$ m in pancake #7 (P7), as reported in [11], roughly corresponding to max (B) and max ($|\varepsilon|$).

- The initial pressures and temperatures at different locations/nodes in the winding and case cooling circuits (see Fig. 2) are summarized in Table 4. The supercritical He pumps provide a total mass flow rate of ~0.13 kg/s to the winding, and 0.1 kg/s to the case cooling channels. The structures are initially in thermal equilibrium with the helium.
- The heat loads q_rp and q_case; these were provided by a separate computation [12] and turn out to be approximately uniform. Their evolution during the fast discharge is shown in Fig. 5.

3.3. Results and discussion

The evolution of the voltage computed on the different pancakes is shown in Fig. 6 (this voltage is obtained by integrating along

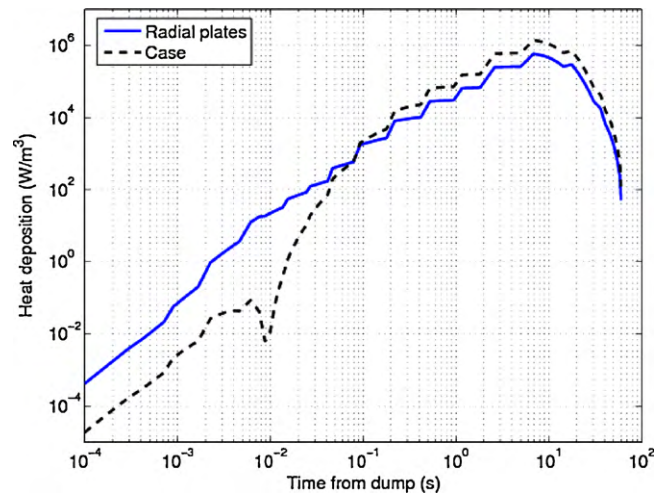

Fig. 5. Time evolution of the power density deposited in the radial plate (solid) and in the case (dashed) during the fast discharge.

Table 4
Initial temperature T and pressure p at selected winding and case circuit locations.

Node	Description	Variable	Value
1	Inlet of pump 1 = outlet of hot cryoline 1 (winding)	T (K) p (MPa)	4.37 0.487
2	Outlet of pump 1 = inlet of control valve 1 (winding)	T (K) p (MPa)	4.48 0.634
3	Inlet of HX 1 = outlet of control valve 1 (winding)	T (K) p (MPa)	4.50 0.626
4	Outlet of HX 1 = inlet of cold cryoline 1 (winding)	T (K) p (MPa)	4.20 0.612
5	Outlet of cold cryoline 1 (winding) = inlet of winding pack	T (K) p (MPa)	4.33 0.599
6	Outlet of winding pack = inlet of hot cryoline 1 (winding)	T (K) p (MPa)	4.35 0.499
7	Inlet of pump 2 = outlet of hot cryoline 2 (case)	T (K) p (MPa)	4.45 0.583
8	Outlet of pump 2 = inlet of control valve 2 (case)	T (K) p (MPa)	4.87 1.233
9	Inlet of HX 2 = outlet of control valve 2 (case)	T (K) p (MPa)	5.38 1.231
10	Outlet of HX 2 = inlet of cold cryoline 2 (case)	T (K) p (MPa)	4.20 0.706
11	Outlet of cold cryoline 2 (case) = inlet of case cooling channels	T (K) p (MPa)	4.21 0.647
12	Outlet of case cooling channels = inlet of hot cryoline 2 (case)	T (K) p (MPa)	4.38 0.641

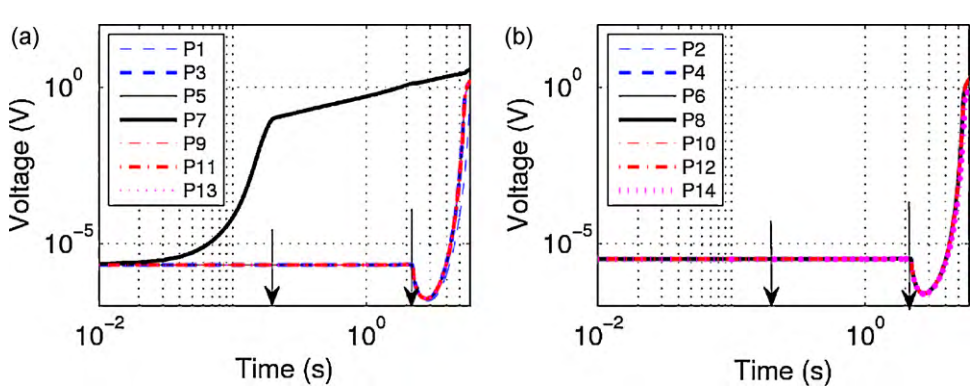

Fig. 6. Voltage evolution of the odd (a) and even (b) pancakes during the quench initiation and propagation, up to the time when the pressure of 18 bar is reached at the conductor inlet. The arrows indicate first the time when the external heating in P7 stops and then the time when the current dump occurs.

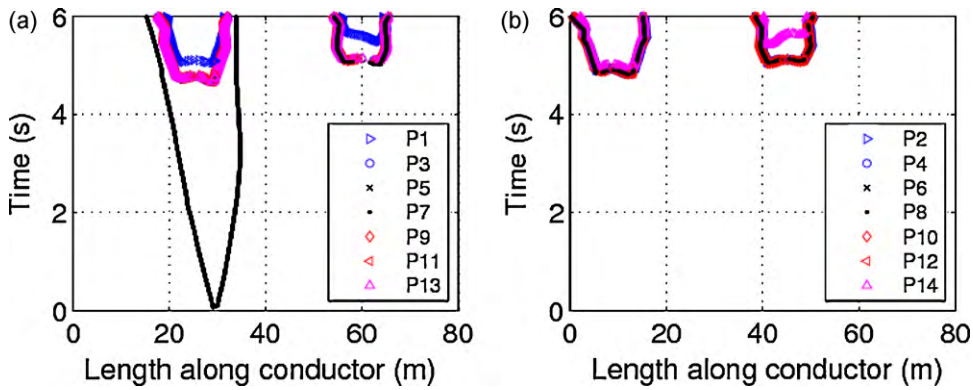

Fig. 7. Normal zone evolution along the odd (a) and even (b) pancakes. The abscissae identify the quench front location ($T = T_{CS}$) at each given time on the ordinates; the conductor locations between two lines at each given time are characterized by $T > T_{CS}$ (normal zone).

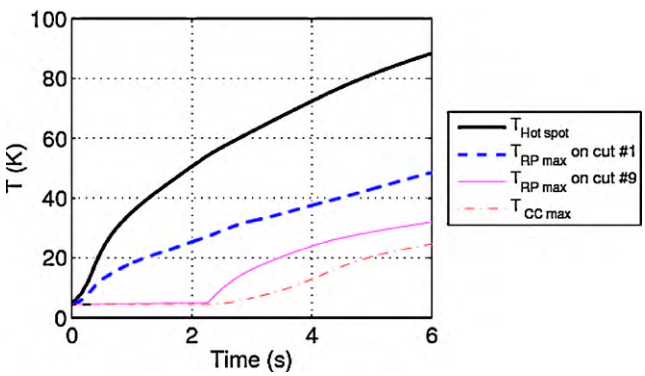

Fig. 8. Evolution of computed temperatures: hot spot (strand) in P7 on cut #1 (thick solid), maximum on structures on cut #1 (dashed), maximum on structures on cut #9 (thin solid), case cooling He on cut #1 (dash-dotted).

each pancake the computed electric field). It is seen that the voltage increases at once in P7 subject to the external heating pulse, while it is initially unchanged in all other pancakes (this value is different from zero because a power law relation is assumed here between the electric field and the current density in the superconductor); at the end of the pulse, $V(t)$ changes slope but keeps increasing because the initial normal zone is now propagating (see Fig. 7) and also the temperature is increasing because of Joule heating (see Fig. 8). At the dump, the initial dominating effect is that of the current reduction, so that the voltage is reduced, but then the eddy current heat deposition in the structures starts becoming dominant and initiates a quench of all other pancakes.

The normal zone propagation computed on the different pancakes is shown in Fig. 7. For each pancake, the part of conductor characterized by an electric field above the critical value of 10 μV/m (i.e. with $T > T_{CS}$) is that included between the two lines (advancing quench fronts). In the odd pancakes other than P7, normal zones are initiated first in the first turn, because of direct heating from the structures. Then, in all odd pancakes, new normal zones arise in the most critical second turn region around $x \sim 60$ m (see Fig. 4). The normal zone in the even pancakes is initiated only by the heating due to the dump, almost simultaneously in the first and second turn, at the minimum temperature margin locations.

The evolution of selected computed temperatures is shown in Fig. 8. On cut #1, across the initially heated region (see Fig. 3), the maximum temperature of the radial plates is significantly lower than that of the P7 conductor, because of their relatively weak thermal coupling; the case cooling He temperature and the structures away from the initially heated region start reacting only after the dump. All temperatures will further increase after the relief valve opens at $t \sim 6$ s (end of the present simulation) because the power released by the dump in the radial plates is still increasing until about 10 s (see Fig. 5) and the Joule power generated in the normal zones is still significant (the transport current at $t = 6$ s is still ~60% of its nominal value).

The evolution of the He pressure computed in the different pancakes on cut #1 is shown in Fig. 9. The pressure in P7 quickly increases during the heating pulse, then more slowly because of the quench power, then again faster because of the dump heating + additional quench power. All the other pancakes start pressurizing only after the dump, first as a consequence of the

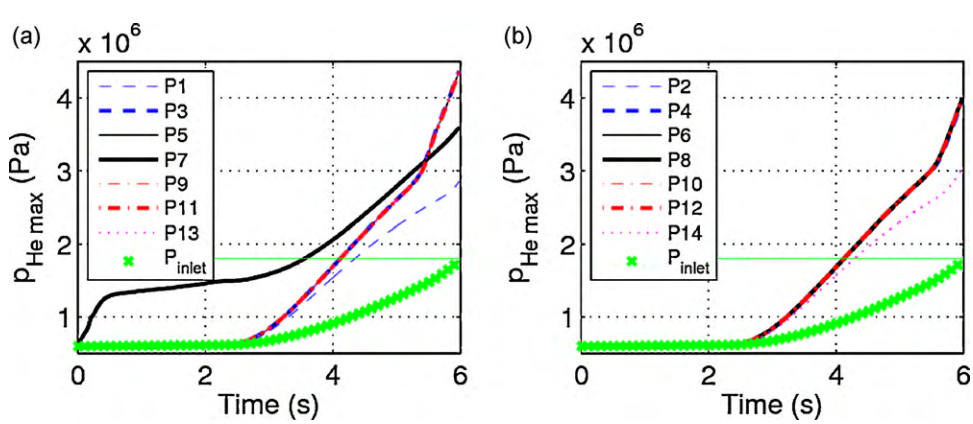

Fig. 9. He pressure evolution on cut #1 for the odd (a) and even (b) pancakes during the quench initiation and propagation. The pressure at the inlet of the coil is also reported, together with the 18 bar threshold (horizontal line).

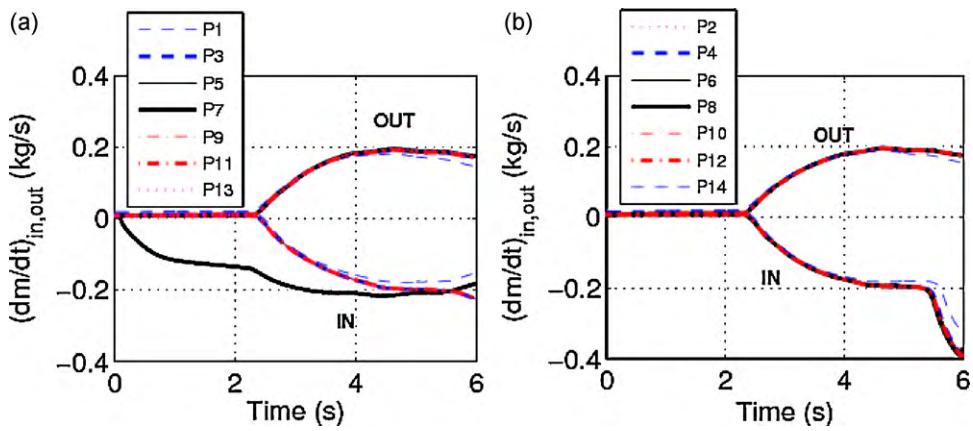

Fig. 10. Mass flow rate evolution of the odd (a) and even (b) pancakes during the quench initiation and propagation, up to the time when the pressure of 18 bar is reached at the conductor inlet.

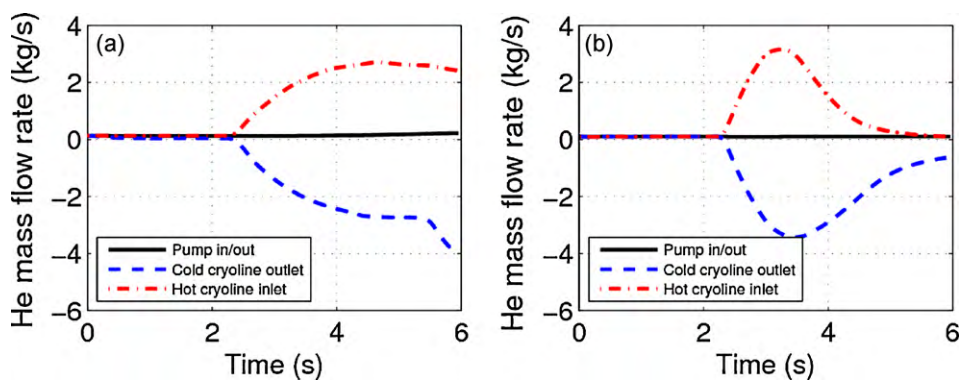

Fig. 11. Mass flow rate evolution in the pump (solid), cold cryoline outlet (dashed) and hot cryoline inlet (dash-dotted) for the winding (a) and case (b) cooling circuits, respectively.

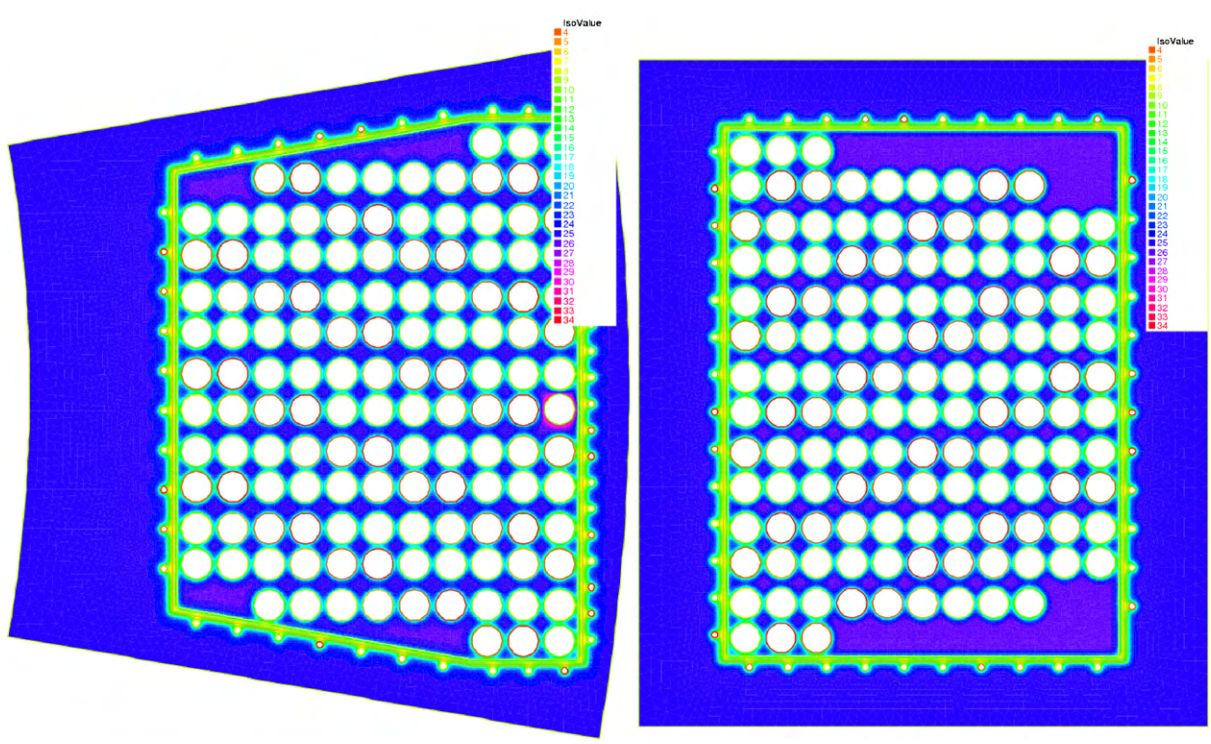

Fig. 12. Temperature distribution computed at the end of the simulation in the structures at the equatorial plane: inboard cut # 3, left, outboard cut #11, right.

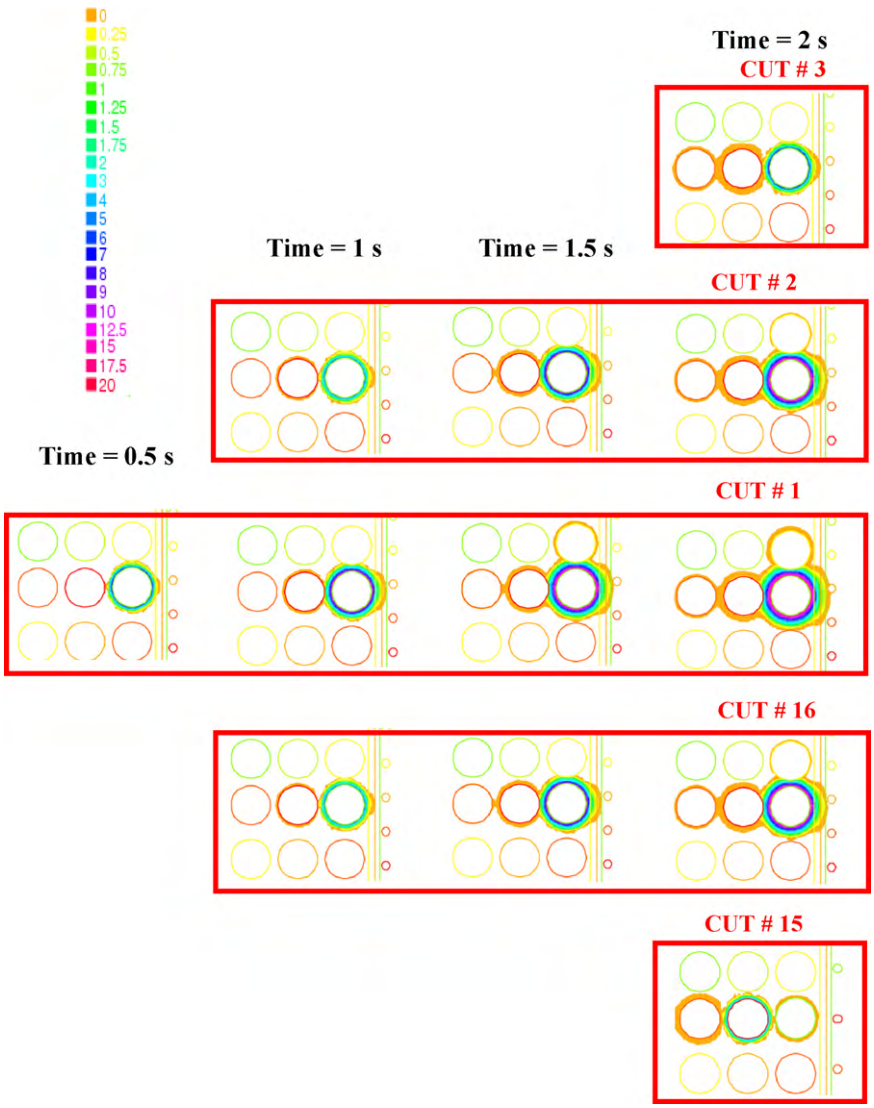

Fig. 13. Zooms of computed 2D maps of the structures temperature increase with respect to the initial condition, at different times before the dump (t = 0.5, 1, 1.5 and 2 s after the pulse) and on different neighbouring cuts. The intersections with the first three turns of pancakes P6-P8 (bottom to top in each subplot) are shown in all cases. Maps on cut #1, across the initially heated zone, are shown at times t = 0.5, 1, 1.5 and 2 s, while maps on all other cuts are shown from the moment they start reacting to the heating.

heating from the structures, then faster due to the quench power. The shortest pancakes P1 and P14 show a slower pressurization.

Also reported in the plot is the pressure p_{inlet} at the inlet of the coil, which grows more slowly because it is representative of the average pressure in the external circuit, which depends on the total volume available. As soon as p_{inlet} reaches 18 bar the simulation stops as this corresponds to the opening of the relief valve, see above. Obviously, the case cooling circuit is also pressurizing during this transient, but at a somewhat lower rate (not shown): the peak pressure reaches ~15 bar at the time when the winding circuit has reached the 18 bar threshold.

The evolution of the inlet and outlet mass flow rate computed on the different pancakes is shown in Fig. 10. In P7, the pulsed heat deposition is sufficient to cause basically at once a flow reversal (inlet backflow), while the outlet flow does not increase until the current dump; the latter feature is related to the fact that the distance along P7 between initially heated region and outlet is ~330 m (see Table 3) and it takes ~2 s (which is close to τ_{delay}) for a sound wave to propagate the information of the pulse to the outlet. As soon as the eddy current heating affects the other pancakes, both outlet flow increase and strong inlet flow reversal occur. When the quench is initiated in the other pancakes the inlet backflow becomes stronger, and the more so in the even pancakes, in view of the proximity of the normal zone to the conductor inlet, see above.

The evolution of the (total) mass flow rate at the inlet of the hot cryolines (downstream of the coil) and at the outlet of the cold cryolines (upstream of the coil) is shown in Fig. 11, for the winding and case cooling circuits, respectively. The mass of hot helium expelled from the winding before the relief valve opens (see Fig. 10a) goes into the rest of the circuit, mainly into the cryolines: Fig. 11a shows that while, for instance, the hot cryoline receives an increasing (positive) mass flow rate from the winding, the pump at its outlet receives more or less always the same mass flow rate, indicating that helium is accumulating in this cryoline.

The solution of the 2D heat conduction problem at the end of the simulation is shown in Fig. 12 on the equatorial plane inboard and outboard cross-sections. We note on the left the local effect of the quench in the initially heated turn of P7, as well as, on both cross-sections, the heating due to the eddy currents induced in the structures after the dump. The cooling effect of both the He flowing in the winding and the He flowing in the 96 case cooling channels

is also highlighted, the zones of the structures further away from these sinks showing the highest temperatures.

Zooms of the computed 2D maps of the structures temperature increase with respect to the initial condition, at different times before the dump (t = 0.5, 1, 1.5 and 2 s after the pulse) and on different, poloidally neighbouring cuts, are shown in Fig. 13.

On the cut #1, across the initially heated section (P7), the temperature increases first around the first turn intersection (t = 0.5 s from the pulse), then inter-turn heat conduction leads to heating around the second turn intersection of P7 (t = 1.0 s from the pulse) and later around the third turn intersection; starting from t = 1.5 s from the pulse, inter-pancake heat conduction leads to heating of neighbouring pancakes, which is however asymmetric because P8 is on the same radial plate and therefore better thermally coupled to P7 than P6. On the poloidally neighbouring cuts to cut #1, namely cuts #2 and #16, quench propagation by He advection along P7 in the downstream and upstream directions, respectively, leads to heating around the first turn intersection (t = 1.0 s from the pulse), then the temperature profile on these cuts evolves similarly to that on cut #1. On the next neighbouring cuts (#3 and #15) the quench arrives later and starts heating the structures around the first turn intersection at a time between 1.5 and 2 s.

4. Conclusions and perspective

The first quantitative demonstration has been given of the capability of the newly developed 4C code to analyze realistic thermal–hydraulic transients of relevance for the operation of the ITER superconducting coils.

The example of a TF quench showed that the 4C code is able to simultaneously and accurately simulate phenomena both at the local (conductor) level and at the global (coil) level.

In perspective it should be interesting to validate the 4C code against the available experimental database and to benchmark it against other existing tools for magnet system analysis.

Appendix: Numerical convergence study

The issue of numerical convergence is fundamental for the demonstration of the accuracy of the present results and of their independence from the chosen numerical parameters. The latter are:

1. The number of cuts N_{CUTS} used for the poloidal discretization of the 3D heat conduction problem in the structures.
2. The mesh used for the discretization of the 2D heat conduction problem in the structures, on each cut, with particular reference to the number of nodes used to discretize the boundaries with the TF conductors.
3. The initial mesh size along the TF conductors.
4. The (fixed) time step adopted for all the model components.

We shall consider below each of the above-mentioned items separately.

For the first item above, a progressive increase of N_{CUTS} has been considered, in order to check the independence of the results on this poloidal discretization. For the problem considered in this paper, the variables which turned out to be most influenced by this feature are the maximum pressure in P7 and the maximum temperature on the cut #1 across the heated region (cut #1, see Fig. 3). The comparison between the results obtained with N_{CUTS} = 2, 4, 8 and 16 is reported in Fig. A1 for the evolution of the above-mentioned variables, showing that with N_{CUTS} = 16 the results reach a reasonable independence on the number of cuts adopted.

For the second item above, the 2D mesh refinement on each cut is controlled by the choice of the number of nodes on the boundaries, where in particular the boundaries between radial plates and conductors are important. For the latter boundaries, 30 edge nodes are used in the present paper. Different discretizations have been considered for the present convergence study and zooms of the

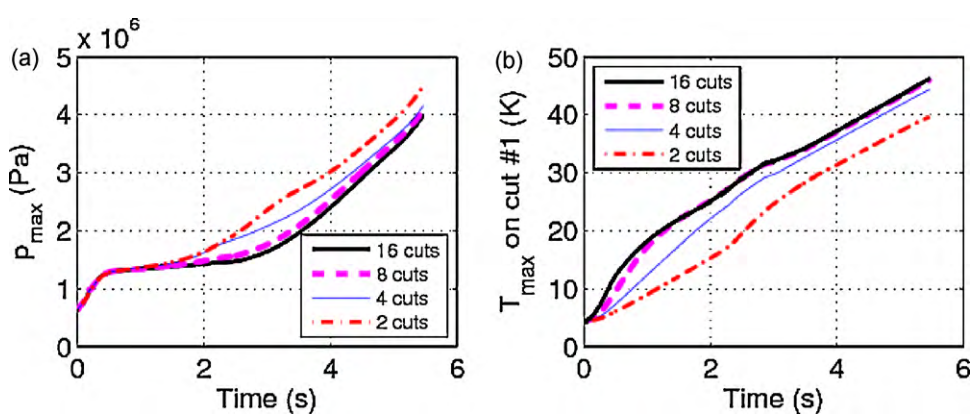

Fig. A1. Maximum pressure in P7 (a) and maximum temperature on cut #1 (b), computed with progressively increasing N_{CUTS}.

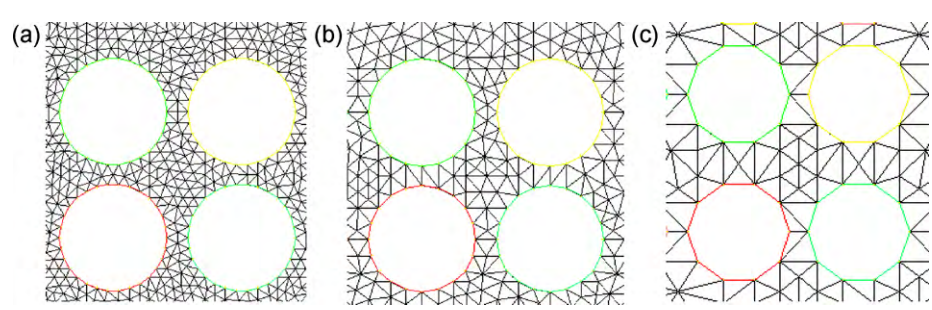

Fig. A2. Zooms of the 2D mesh resulting from different discretizations of the boundaries between radial plates and conductors: (a) 30 nodes, (b) 20 nodes, and (c) 10 nodes.

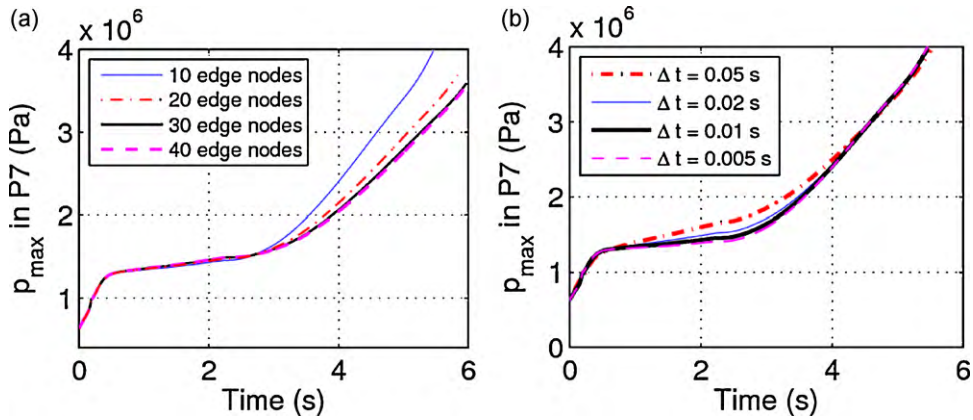

Fig. A3. Maximum pressure in P7 computed with 16 cuts: (a) with an increasing number of nodes on the conductor edges and (b) with decreasing value of the time steps.

resulting 2D meshes are shown in Fig. A2. In Fig. A3(a) we show that 30 edge nodes are indeed sufficient for grid independence.

For the third item above, the initial number of nodes in the conductor shows a negligible effect on all variables, in view of the adaptive mesh adopted in the quench propagation analysis.

For the fourth item above, a time step of 0.01 s is chosen for all the components of the model. Fig. A3(b) shows that this guarantees the convergence of the results on the maximum pressure evolution in P7.

References

[1] D. Bessette, N. Shatil, E. Zapretilina, Simulations of the ITER toroidal field coil operation with the VINCENTA code, IEEE Trans. Appl. Supercond. 16 (2006) 795–798.
[2] R. Zanino, S. DePalo, L. Bottura, A two-fluid code for the thermohydraulic transient analysis of CICC superconducting magnets, J. Fusion Energy 14 (1995) 25–40.
[3] L. Savoldi, R. Zanino, M&M: Multi-conductor Mithrandir code for the simulation of thermal–hydraulic transients in superconducting magnets, Cryogenics 40 (2000) 179–189.
[4] R. Zanino, N. Mitchell, L. Savoldi Richard, Analysis and interpretation of the full set (2000–2002) of Tcs tests in conductor 1A of the ITER central solenoid model coil, Cryogenics 43 (2003) 179–197.
[5] R. Zanino, L. Savoldi Richard, Performance evaluation of the ITER toroidal field model coil phase I. Part 2. M&M analysis and interpretation, Cryogenics 43 (2003) 91–100.
[6] L. Savoldi Richard, F. Casella, B. Fiori, R. Zanino, Development of the Cryogenic circuit conductor and coil (4C) code for thermal–hydraulic modeling of ITER superconducting coils, in: H.-M. Chang, al. et (Eds.), Proceedings of the 22nd International Cryogenic Conference (ICEC22), 2009, pp. 619–624.
[7] L. Savoldi Richard, F. Casella, B. Fiori, R. Zanino, The 4C code for the cryogenic circuit conductor and coil modeling in ITER, Cryogenics 50 (2010) 167–176.
[8] N. Mitchell, D. Bessette, R. Gallix, C. Jong, J. Knaster, P. Libeyre, et al., The ITER magnet system, IEEE Trans. Appl. Supercond. 18 (2008) 435–440.
[9] ITER Technical Basis, Cap. 3.2. Cryoplant and Cryodistribution, 2001.
[10] N. Mitchell, Summary, assessment and implication of the ITER model coil test results, Fusion Engineering and Design 66–68 (2003) 971–993.
[11] L. Savoldi Richard, R. Zanino, Stability analysis of the ITER TF conductor, Adv. Cryo. Eng. 53 (2008) 1269–1276.
[12] D. Bessette, "Current Decay during TF Fast Discharge", https://user.iter.org/?uid=2NKRCR.